Specific targeting of ovarian tumor-associated macrophages by large, anionic nanoparticles

Tom Haber[a], Yvonne R. Cornejo[a,b], Soraya Aramburo[c], Linda Flores[c], Pengpeng Cao[a], Alice Liu[a,b], Rachael Mooney[c], Megan Gilchrist[c], Revathiswari Tirughana[c], Ugochi Nwokafor[c], Wafa Abidi[a], Ernest Han[d], Thanh Dellinger[d], Mark T. Wakabayashi[d], Karen S. Aboody[b,c,1], and Jacob M. Berlin[a,b,1,2]

[a]Department of Molecular Medicine, City of Hope and Beckman Research Institute, Duarte, CA 91010; [b]Irell and Manella Graduate School of Biological Sciences, City of Hope and Beckman Research Institute, Duarte, CA 91010; [c]Department of Developmental and Stem Cell Biology, City of Hope and Beckman Research Institute, Duarte, CA 91010; and [d]Department of Surgery, City of Hope, Duarte, CA 91010

Edited by Catherine J. Murphy, University of Illinois at Urbana–Champaign, Urbana, IL, and approved June 17, 2020 (received for review October 7, 2019)

Immunotherapy is emerging as one of the most effective methods for treating many cancers. However, immunotherapy can still introduce significant off-target toxicity, and methods are sought to enable targeted immunotherapy at tumor sites. Here, we show that relatively large (>100-nm) anionic nanoparticles administered intraperitoneally (i.p.) selectively accumulate in tumor-associated macrophages (TAMs). In a mouse model of metastatic ovarian cancer, fluorescently labeled silica, poly(lactic-*co*-glycolic acid), and polystyrene nanoparticles administered i.p. were all found to selectively accumulate in TAMs. Quantifying silica particle uptake indicated that >80% of the injected dose was in TAMs. Particles that were smaller than 100 nm or cationic or administered intravenously (i.v.) showed no TAM targeting. Moreover, this phenomenon is likely to occur in humans because when freshly excised human surgical samples were treated with the fluorescent silica nanoparticles no interaction with healthy tissue was seen but selective uptake by TAMs was seen in 13 different patient samples. Ovarian cancer is a deadly disease that afflicts ∼22,000 women per year in the United States, and the presence of immunosuppressive TAMs at tumors is correlated with decreased survival. The ability to selectively target TAMs opens the door to targeted immunotherapy for ovarian cancer.

intraperitoneal therapy | tumor-associated macrophages | nanoparticles | ovarian cancer

Ovarian cancer is a deadly disease that afflicts ∼22,000 women per year in the United States. Over 70% of newly diagnosed patients with epithelial ovarian cancer are found in advanced stages with metastasis commonly noted within the abdominal/pelvic cavity. In the past 10 y, 5-y survival rates (∼40%) have not significantly improved with standard surgery and chemotherapies (1, 2). There is a clear need for the development of new treatments for this disease.

Checkpoint inhibitor therapy to unrestrain T cells has been transformative for treating tumors that are immunologically "hot," such as melanoma (3). However, initial results for treating ovarian cancer with only intravenous (i.v.) dosing of antibodies inhibiting the immune checkpoint programmed cell death 1 (PD-1) or its ligand (PD-L1) were quite modest, with an average response rate of 10 to 15% and a disease control observed in less than half of the patients and frequent later onset of immune checkpoint blockade resistance (5). This suggests that many ovarian tumors are intrinsically immunologically "cold" and locally immunosuppressive. The key to enabling immunotherapy for ovarian cancer may be overcoming this barrier and selectively targeting tumors for immunoactivation without causing inflammation throughout the rest of the intraperitoneal (i.p.) cavity (4).

Tumor-associated macrophages (TAMs) are well recognized as potential targets in oncology due to their tumor-supportive properties, including their role in rendering the tumor microenvironment immunosuppressive (5–7). In particular for ovarian cancer, the presence of TAMs that are tumor-supportive/antiinflammatory (M2 polarized) is negatively correlated with patient survival (1). TAMs have even been directly implicated in facilitating ovarian cancer metastases by supporting tumor spheroid formation by detached cancer cells (8). A targeted method for delivering therapeutic payloads to ovarian TAMs would be a significant advance and open the door to selective immunotherapy. However, no such method currently exists for targeting ovarian TAMs relative to macrophages elsewhere in the body, and perhaps as a result, there are no clinical trials specifically targeting TAMs in ovarian cancer.

Nanoparticles (NPs) are emerging as useful vehicles for delivering therapeutic and imaging cargo to TAMs. To date, studies have focused on i.v. dosing of NPs to treat or image solid tumors and the overall efficiency of delivery is modest (9). Previously, we had observed that when fluorescent silica NPs (SiNPs) that had no surface functionalization were administered i.p., they selectively accumulated on the surfaces of tumors in a mouse model of abdominal metastatic ovarian cancer (10). Here, we show that this tumor accumulation is actually driven by uptake by ovarian TAMs and is a result of both the route of administration and the size and charge of the NPs. Systematic variation of SiNP parameters demonstrated that selective labeling of tumors occurs over several days and is dependent on the particles being

Significance

Tumor-associated macrophages (TAMs) are abundant in tumor microenvironments and are predominantly immunosuppressive. The ratio between immunosuppressive M2 TAMs and proinflammatory M1 TAMs correlates with worse outcomes for many cancers, including ovarian cancer. TAMs are potential targets for immunotherapy, and here we show that, when relatively large (>100-nm) anionic nanoparticles are administered intraperitoneally (i.p.), they selectively accumulate in TAMs with high efficiency (>60% of injected dose). The composition of particles that achieve this targeting appears to be quite flexible. Thus, based on our results, many formulations can now be tested for targeted immunotherapy of ovarian cancer and other cancers of the i.p. cavity.

Author contributions: T.H., Y.R.C., P.C., R.M., K.S.A., and J.M.B. designed research; T.H., Y.R.C., S.A., L.F., P.C., A.L., R.M., M.G., R.T., U.N., and W.A. performed research; E.H., T.D., and M.T.W. contributed new reagents/analytic tools; T.H., Y.R.C., P.C., A.L., R.M., M.G., R.T., U.N., W.A., K.S.A., and J.M.B. analyzed data; and T.H., K.S.A., and J.M.B. wrote the paper.

The authors declare no competing interest.

This article is a PNAS Direct Submission.

[1]K.S.A. and J.M.B. contributed equally to this work.

[2]To whom correspondence may be addressed. Email: jacobberlincoh@gmail.com.

This article contains supporting information online at https://www.pnas.org/lookup/suppl/doi:10.1073/pnas.1917424117/-/DCSupplemental.

First published July 30, 2020.

relatively large (>200 nm) and anionic, and being administered i.p. This behavior extends to NPs of other composition, as large and anionic NPs composed of either poly(lactic-*co*-glycolic acid) (PLGA) or polystyrene both also accumulated in TAMs when administered i.p. The accumulation of SiNPs in ovarian TAMs results in an increase in TAMs at the metastatic tumor sites and may bias these TAMs to the M1 phenotype. Finally, we close this manuscript by demonstrating that not only do the NPs selectively label tumor surfaces in mouse models of abdominal metastatic ovarian cancer but also selectively label human tumor surfaces (and not normal tissues) in freshly excised surgical samples. Immunohistochemical staining confirmed that this tumor selectivity is also mediated by macrophages in the human tissue. The highly specific delivery of NPs of appropriate size and charge into ovarian TAMs offers a unique opportunity for future development of targeted immunotherapy as a number of different compositions of NPs may now be explored with great confidence in their targeting ability.

Results and Discussion

In a pilot study using a metastatic mouse model of abdominal (stage III) ovarian cancer (human OVCAR8.EGFP cell line injected i.p.), we found that when nonfunctionalized SiNPs with a hydroxyl surface bearing an internal red fluorescent dye were administered i.p., they selectively targeted ovarian tumor metastases, completely sparing nontumor tissues (for full characterization of all NPs used in this manuscript, see Table 1). For these studies, tumor-bearing mice were euthanized 4 d post-SiNP injection, and the organs in the i.p. cavity were removed and observed with a fluorescent wide-field imaging system. This imaging demonstrated the SiNPs selectively localized to metastatic tumor sites (Fig. 1*A*). Tumors and adjacent healthy tissue were then dissected and prepared for confocal imaging, which further confirmed that the SiNPs only accumulated on tumor surfaces but not on normal (nontumor) tissues (Fig. 1*B*). It also can be seen that even submillimeter tumors (0.5 mm) can be detected by these SiNPs. In order to quantify this tumor labeling, all red (NPs) and green (tumors) signals from images taken by the fluorescent wide-field imaging system were calculated as ellipses, analyzed as particles, and merged using ImageJ software. Overlay of red and green, red only, and green only signals higher than the threshold (signals higher than the background and more than 10 pixels in the ellipse) were counted (Fig. 1*C*). It was found that, in average, 94% of tumors were labeled with red SiNPs and only 3% of locations were labeled with the SiNPs but had no tumor signal.

Table 1. NP characterization summary: Size, dispersity, and charge of the different NPs

Name	Hydrodynamic diameter ± SE, nm	Dispersity ± SE	ζ-Potential ± SE, mV
10-nm SiNP	24.6 ± 4.1	0.333 ± 0.010	−24.22 ± 0.98
50-nm SiNP	54.7 ± 1.4	0.167 ± 0.018	−23.19 ± 0.71
200-nm SiNP	194.8 ± 2.1	0.041 ± 0.023	−37.12 ± 1.39
500-nm SiNP	443.9 ± 4.7	0.042 ± 0.026	−54.59 ± 0.80
1,000-nm SiNP	982.9 ± 11.8	0.049 ± 0.034	−73.71 ± 1.09
Gold@SiNP	207.8 ± 2.2	0.034 ± 0.020	−45.01 ± 0.65
PLGA NP	398.0 ± 4.9	0.355 ± 0.026	−21.89 ± 0.97
Polystyrene NP	798.0 ± 7.8	0.014 ± 0.010	−21.32 ± 3.20
Hydroxyl-SiNP	443.9 ± 4.7	0.042 ± 0.026	−55.74 ± 0.46
Amine-SiNP	464.4 ± 3.2	0.135 ± 0.042	+22.88 ± 0.79
PEG-SiNP	397.3 ± 5.6	0.181 ± 0.021	+10.58 ± 0.72

A survey of historical literature revealed that several other groups had also observed tumor-specific accumulation of untargeted NPs administered i.p., including PLGA microparticles loaded with fluorophores or paclitaxel (11); NPs composed of an amphiphilic copolymer of 2-methacryloxyethyl phosphorylcholine and *n*-butyl methacrylate loaded with paclitaxel (12, 13); neutron-activatable holmium-containing mesoporous SiNPs (14); and, most recently, expansile NPs composed of a pH-responsive polymer (15). Interestingly, in all of these cases, despite using NPs composed of different materials, all of the NPs were larger than 100 nm, negatively charged, and i.p. injected, and their accumulation on the tumor surface increased with time (11, 12, 14).

Using our SiNPs as a tunable system, we systematically investigated the charge, size, and route of administration to determine how each parameter affected the accumulation at the tumor site. We began by testing the i.p. injection of SiNPs with three different surfaces: hydroxyl (negative charge: ζ-potential, −55.74 mV), amines from coating the hydroxyl particles with (3-aminopropyl)triethoxysilane (positive charge: ζ-potential, +22.88 mV), and poly(ethylene glycol) (PEG) from reacting the amine particles with PEG-*N*-hydroxysuccinimide (less positive effective charge: ζ-potential, +10.58 mV) (*SI Appendix*, Fig. S1 *A* and *B* and Table 1). It was found that the cationic, amine functionalized SiNPs had minimal tumor targeting, the PEGylated SiNPs had modest tumor targeting, and the anionic, hydroxyl SiNPs had highly selective tumor targeting (*SI Appendix*, Fig. S1 *C* and *D*).

The impact of SiNP size was next investigated using five different sizes of the red fluorescent-labeled hydroxyl SiNPs: 10, 50, 200, 500, and 1,000 nm (Table 1). In addition to wide-field fluorescence imaging (*SI Appendix*, Fig. S2*A*), we used a dissection macroscope that afforded much-improved resolution and sensitivity while maintaining a relatively large field of view (3 cm in diameter). For this imaging technique, there is a background red signal from the organs. To account for this, the threshold for red fluorescence intensity in all images was set above that measured in the no-SiNP control (Fig. 2). In order to quantify these results, fluorescence colocalization analysis was performed by using ImageJ software. Results demonstrated minimal tumor targeting for particles ≤50 nm, and significantly higher tumor coverage with 500-nm SiNPs compared to the 200 SiNPs (Fig. 2 and *SI Appendix*, Fig. S2 *A–C*). Although 500-nm and 1,000-nm SiNPs showed no significant difference in tumor coverage, we decided to continue only with the 500-nm SiNPs since the 1,000-nm SiNPs coverage was not significantly higher than the 200-nm group and due to high variance in the 1,000-nm SiNPs results (*SI Appendix*, Fig. S2*C*). One limitation of this experiment was that surface charge was highly correlated with diameter (the particles with HD sizes measured by dynamic light scattering [DLS] of 24.6, 54.7, 194.8, 443.9, and 982.9 nm had charges as measured by ζ-potential of −24.22, −23.19, −37.12, −54.59, and −73.71 mV), leaving open the possibility that size plays little or no role. However, as is discussed in more detail later in this manuscript, i.p. injection of either large polystyrene NPs ∼800 nm in diameter and with a surface charge of −21.32 mV or large PLGA NPs 398 nm in diameter with a surface charge of −22 mV also resulted in selective uptake in ovarian TAMs (*SI Appendix*, Fig. S8 *A* and *B*). Since the charges of the polystyrene and PLGA NPs were similar to the 10 nm (that measured as HD of 24.6 nm) but still showed selective accumulation, we favor the hypothesis that the NPs must be both large and anionic to display selective accumulation. The size dependence of tumor targeting could correlate with the circulation time of the NPs in the i.p. cavity, as Feng et al. (16) showed that liposomes smaller than ∼200 nm that were administered i.p. were able to traverse into the bloodstream, while liposomes of size ∼400 nm showed negligible uptake into the bloodstream and their retention was limited to

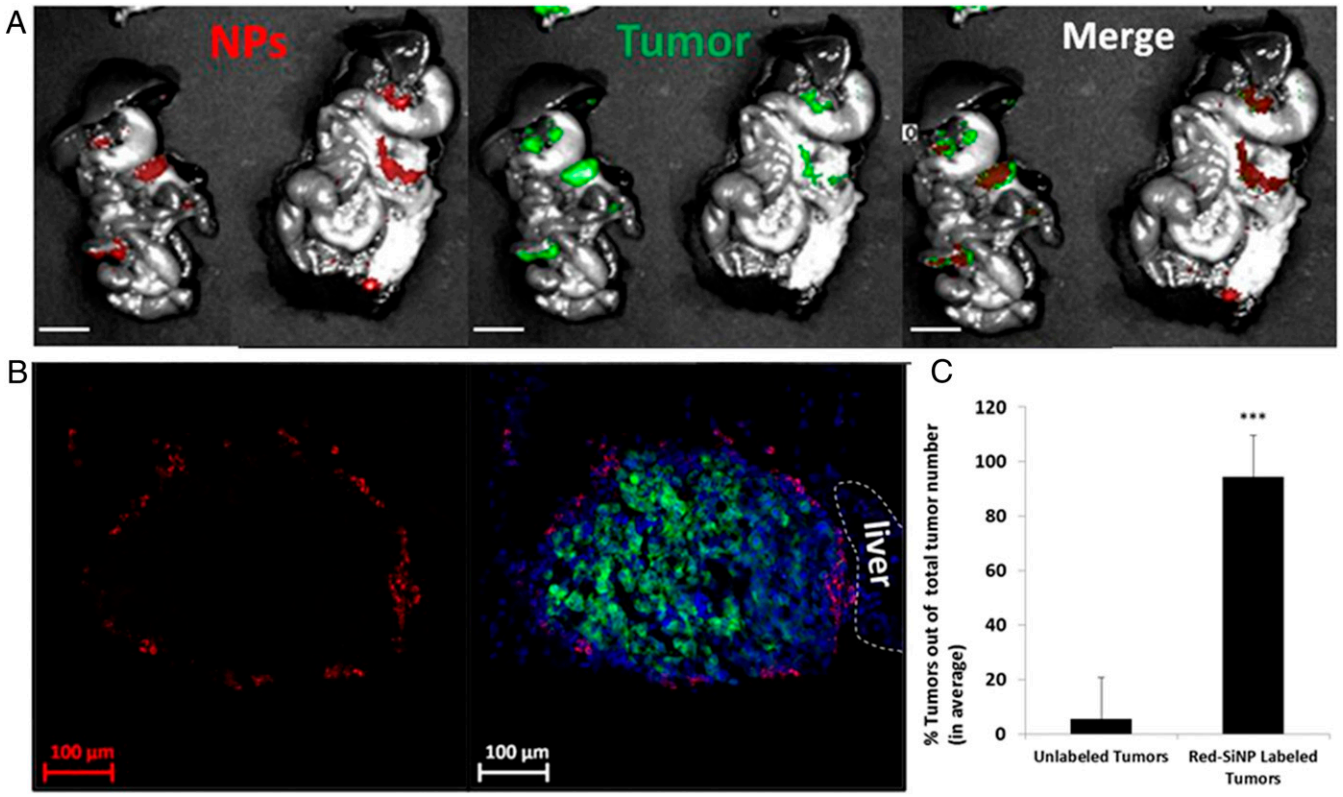

Fig. 1. Red fluorescent-labeled SiNPs demonstrate selective tumor targeting when injected i.p. into a metastatic ovarian cancer mouse model. EGFP-expressing human metastatic ovarian cancer cells (OVCAR8) were injected i.p. After 21 d, the red fluorescent-labeled SiNPs were injected i.p., and then 4 d later the animals were euthanized and i.p. cavity organ block removed for imaging. (*A*) Wide-field imaging (Spectral Ami-X) of the organ block demonstrates selective accumulation of SiNPs (red) at (metastatic) ovarian tumor foci (green). (Scale bar: 1 cm.) (*B*) Confocal images of the sectioned metastatic tumors (SiNPs, red; tumors, green/dense blue nuclei. (Scale bar: 100 μm.) (*C*) Quantification of tumor labeling by NPs shows that on average 94% of tumors are labeled with NPs; error bars are presented as mean ± SD; $P < 0.001$ (two-tailed Student's *t* test) (using ImageJ software, NIH; $n = 49$).

the peritoneum cavity and the surrounding areas. Thus, particularly for hard NPs, there may be a size above which they are predominantly constrained to the i.p. cavity following i.p. injection and this then enables predominant uptake by TAMs. To further investigate whether i.p. circulation was important for tumor targeting, we compared the effect of i.p. versus i.v. route of SiNP administration. Examination of the tumors and i.p. organs 4 d post-i.v. injection of the 500-nm SiNPs (1 mg NPs/mL) with a hydroxyl surface showed lack of red fluorescent signal in the peritoneal cavity, as can be seen from the images taken with a wide-field imaging system, and from the dissection macroscope images (*SI Appendix*, Fig. S3).

Next, the timing of SiNP localization to the tumors was evaluated by killing mice 1 h, 5 h, 24 h, and 4 d after i.p. injection of SiNPs. The i.p. cavity organ blocks were removed and imaged by a wide-field imaging system. As seen in Fig. 2*B*, there was no to minimal red signal at tumor sites with short incubation times (1 and 5 h). SiNP localization to tumors started to be visible after 24 h, and the highest tumor biodistribution was detected after 4 d, with SiNPs seen selectively colocalized to tumors in all mice.

To determine whether signal from the tumors accounted for most of the injected SiNP dose or whether we were missing signal from SiNPs that may have accumulated in other off-target tissues where the SiNPs were too far from the organ surface for detection by fluorescent imaging, we both performed whole-animal fluorescent imaging using an instrument (CryoViz; BioInVision) built to serially section through the entire intact carcass and capture a fluorescent image after each slice (Fig. 3*A*), and we also used inductively coupled plasma mass spectrometry (ICP-MS) to precisely quantify the distribution of SiNPs with a gold core (Au@SiNPs) (Fig. 3*B*, Au@SiNP particle characterization in *SI Appendix*, Fig. S4 and Table 1).

For the whole-animal serial-section, fluorescent imaging performed using CryoViz, tumor-bearing and healthy mice were injected with red fluorescent 500-nm SiNPs with a hydroxyl surface (Table 1). In the tumor-bearing mice, the red fluorescence was exclusively observed in the i.p. cavity and was predominantly colocated with tumors (Fig. 3*A1*). An untreated tumor-bearing mouse was also imaged and showed negligible red fluorescence signal, as expected (*SI Appendix*, Fig. S13). Interestingly, in healthy mice, almost no red fluorescent signal was observed, suggesting that the particles were actually excreted within 4 d in the healthy animal (Fig. 3*A2*).

The use of a gold core allows for more precise measurement of NP distribution by ICP-MS, since there is no background gold signal in tissue but there is a background silica signal. The largest particles we were able to produce with a gold core were 50-nm gold NPs coated with a 75-nm-thick Si shell to yield particles ~200 nm in diameter. While this is smaller than the 500-nm red fluorescent SiNPs used in the prior experiments, based on the size dependence in Fig. 2, the 200-nm Au@SiNPs would likely represent a worst-case scenario for biodistribution. The Au@SiNPs were injected i.p. to three tumor-bearing mice, and i.p. organ blocks were harvested 4 d later. Biodistribution was determined by measuring gold by ICP-MS (Fig. 3*B*). Surprisingly, 84.8 ± 8.5% of the injected dose was found at the tumors.

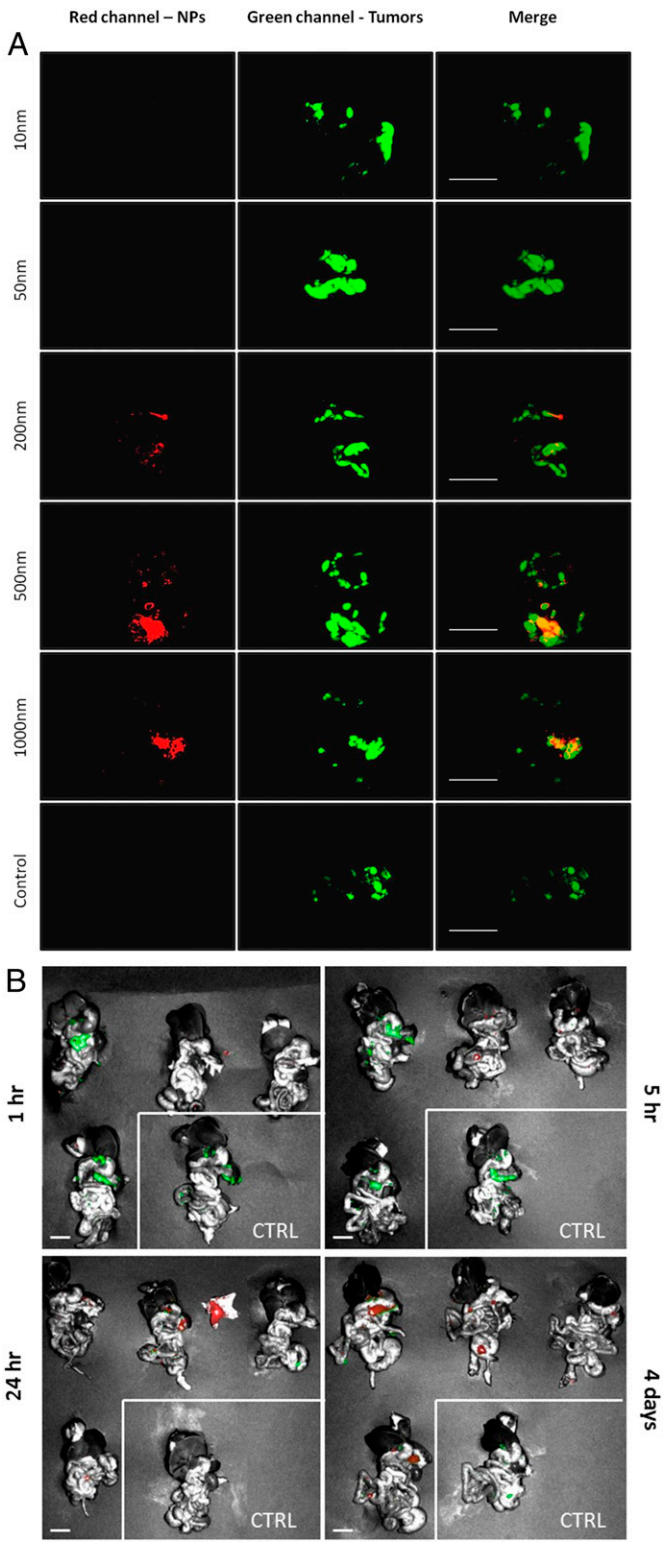

Fig. 2. The effect of SiNP size and timing on the selective tumor targeting. (*A*) Leica Z16 dissection macroscope images of i.p. cavity organ block 4 d after the i.p. injection of 10-, 50-, 200-, 500-, and 1,000-nm red fluorescent-labeled SiNPs with a hydroxyl surface and no SiNP control. (*Left*) SiNPs, red; (*Middle*) tumor cells, green; (*Right*) merged images showing overlap orange/yellow. (Scale bar: 1.0 cm.) (*B*) Spectral Ami-X wide field images of i.p. cavity organ blocks 1 h, 5 h, 24 h, and 4 d after the i.p. injection of 500-nm red fluorescent-labeled SiNPs. SiNPs, red; tumors, green. No SiNPs control indicated by white border. (Scale bar: 1.0 cm.)

All signals from other organs were below the limit of ICP-MS detection. Collectively, the data described thus far showed that when appropriately sized (>100 nm) and nonfunctionalized (hydroxyl surface) SiNPs are administered i.p., highly efficient and selective labeling of ovarian tumors is achieved 4 d later.

We next explored why SiNPs with just a hydroxyl surface were localizing to tumors so selectively. Given our observations that SiNPs accumulate at high density only at the surface of tumors, the necessity of i.p. administration, and tumor localization taking several days, we hypothesized that the NPs are circulating in the i.p. cavity and being taken up by cells. If the targeting instead occurred through either extravasation from blood vessels or attachment to the extracellular matrix, we would expect that i.v. administration or shorter time periods would work, respectively. To further clarify the location of the SiNPs at the tumor foci, tumors from treated mice were sectioned and imaged by confocal microscopy at high magnification. Interestingly, the red

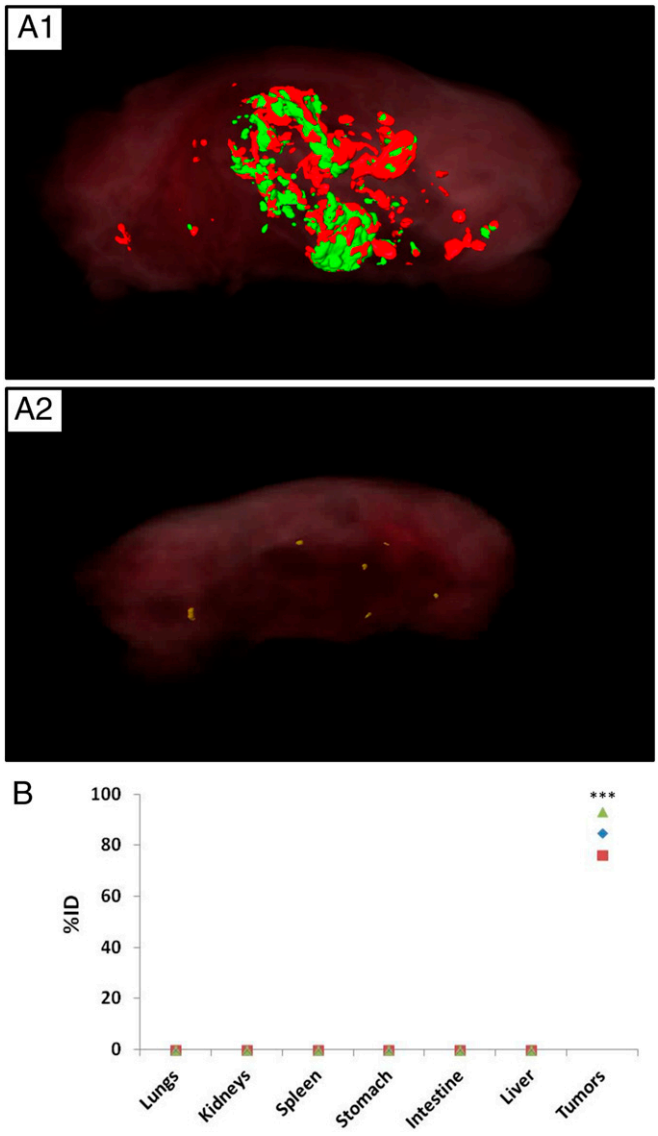

Fig. 3. Kinetics of attachment and biodistribution of the SiNPs. (*A*) CryoVis reconstructed images of the whole mouse 4 d after injection of SiNP (red) in (*A1*) mice bearing EGFP-labeled ovarian tumors (green) or (*A2*) healthy control mice. (*B*) ICP-MS evaluation of biodistribution, showing the percentage of injected Au@SiNPs dose in major organs harvested after 4 d ($n = 3$ mice; each mouse is represented with a different shape); $P < 0.001$.

SiNP signal was found to be clearly located inside cells but did not colocalize with the GFP-expressing cancer cells (Fig. 4*A*). Flow cytometry analysis showed that just 2.1% of tumor cells (green) contained SiNPs (red) (Fig. 4*B*). In contrast, 72% of cells containing SiNPs were also positive for TAM markers CD45, CD11b, and F4/80 (Fig. 4*C*). Indeed, when the total population of TAMs was evaluated, 87% were found to contain SiNPs (Fig. 4*D*). It is clear that tumor targeting is actually driven by very efficient uptake by ovarian TAMs. Interestingly, there is also a trend that SiNPs alone may bias the TAMs toward an M1 phenotype—although additional work will be required to confirm this (Fig. 4*E*). Additionally, treatment with SiNPs leads to an increase in the number of TAMs at the tumor sites (Fig. 4*F*). The colocalization of SiNPs with TAMs is readily apparent upon confocal imaging (Fig. 4*G*, lack of staining for GR-1 is shown in *SI Appendix*, Fig. S5 and staining controls are in *SI Appendix*, Fig. S6).

We next probed how generalizable was targeting of ovarian TAMs by large, anionic NPs. It was found that the phenomenon extends to other ovarian tumor models, as similar results for 500-nm SiNPs were observed in a mouse model generated using SKOV-3 cells (*SI Appendix*, Fig. S7 *A* and *B*). Targeting was also observed for other classes of NPs, as i.p. injection of either large polystyrene NPs ∼800 nm in diameter and with a surface charge of −21.32 mV or large PLGA NPs 398 nm in diameter as measured by DLS and with a surface charge of −22 mV resulted in selective uptake in ovarian TAMs (*SI Appendix*, Fig. S8 *A* and *B* and Table 1). Moreover, selective TAM targeting occurs in human samples as well. Freshly excised tumor and nonmalignant tissue samples were obtained from patients and incubated ex vivo with fluorescently labeled SiNPs for 1 h, and 1, 4 and 7 d. Similar to the results in mice, the accumulation of SiNPs at tumor foci increased with incubation time, peaking at 4 d, with a strong signal still present at 7 d (*SI Appendix*, Fig. S5*A*). Notably, in all 13 cases (additional examples in *SI Appendix*, Fig. S9), SiNPs selectively localized to the surface of metastatic tumor samples (collected from various locations including the diaphragm, omentum, colon, and rectum) with minimal labeling of matched healthy tissue samples. Moreover, only the anionic SiNPs targeted the human tumors (*SI Appendix*, Fig. S10), and 500 nm was the optimal size (*SI Appendix*, Fig. S11). Immunofluorescence staining confirmed that this tumor accumulation was again driven by TAM ($CD11b^+$, $CD14^+$, and $CD68^+$) uptake (Fig. 5*B*).

Conclusion

In conclusion, we have demonstrated that highly efficient targeting of TAMs is achieved by injecting large, anionic NPs i.p. This phenomenon is relatively general as it was observed for two different mouse models of metastatic ovarian cancer (OVCAR8, SKOV3) as well as in multiple freshly excised human tumors and occurs for at least three different compositions of NPs: rigid, inorganic SiNPs; rigid, organic polystyrene NPs; and soft, organic PLGA NPs. In the case of the SiNPs, multiple methodologies were used to evaluate the targeting. Using wide-field fluorescent microscopy, it was found that >80% of fluorescently detectable tumors were labeled with observable NP signal, and that the NP signal increase over time following injection, becoming prominent after 24 h and remaining at or above that level after 4 d. It is possible, even likely, that for other materials this time series will vary and researchers should perform quantitative time series studies to identify the accumulation behavior of specific NPs. Wide-field fluorescent microscopy was also used to evaluate the size dependence of NP accumulation, and it was found that for the SiNPs, a size above 100 nm was required and 500 nm was optimal. For the polystyrene NPs (∼800 nm) and PLGA NPs (∼400 nm), only one size was evaluated. Returning to the SiNPs, whole-animal fluorescent imaging using serial sectioning and ICP-MS of harvested organs were used to evaluate the distribution of the NPs after 4 d and the only signal was observed in the tumors, with >60% of the injected dose found there. Finally, a combination of flow cytometry and fluorescent immunohistochemistry was used to identify that the NPs were almost exclusively taken up by TAMs at the tumors (87% of TAMs contained NPs), with little signal in the cancer cells (2% of cancer cells contained NPs).

The results here suggest that a wide variety of NP materials can be used to target TAMs in the i.p. cavity with extremely high efficiency—a level never observed for i.v. administration. Furthermore, previous reports have also identified selective tumor targeting for i.p.-injected NPs, although in those reports, selective tumor targeting was attributed to the specific NP characteristics and presumed to involve binding or internalization by cancer cells. Based on our data, we speculate that many or all of these examples are mediated by selective uptake into TAMs as well, which would provide further examples of the generality of this result. This is highly relevant as immunotherapy has emerged as one of the most important and effective frontiers for oncology and the ability to selectively deliver therapeutics to TAMs could be transformative for treatment of abdominal tumors. We encourage researchers in the field to test a wide range of targeted immunotherapies to identify promising leads for translation to the clinic for treating ovarian cancer and potentially also other tumors that have spread to the i.p. cavity.

Materials and Methods

General.

NPs characterization. The concentration of NPs and their size (mean diameter) were measured using the NanoSight NS300 and analyzed with the NP tracking analysis software (Malvern NanoSight NS300 instrument; NTA software). Measurements were obtained by performing three runs of 60 s each; sample flow rate was controlled and kept constant (speed = 30) during the acquisition using a syringe pump.

DLS and ζ-potential measurements were performed on a Brookhaven 90 Plus/BI-MAS Instrument (Brookhaven Instruments). DLS measurements were obtained by performing five runs at 30 s per run, and ζ-potential measurements were obtained by performing 10 runs with 30 cycles per run. ζ-Potential buffer and salt concentration: NPs were measured in 10 mM sodium chloride (NaCl) in dH_2O solution.

Transmission electron microscopy (TEM) images were obtained with an FEI Tecnai T12 transmission electron microscope at an accelerating voltage of 120 keV, and images were taken with a Gatan Ultrascan 2K CCD camera. The NP samples were imaged on 300 mesh carbon/formvar coated grids (Ted Pella).

Scanning electron microscopy images were obtained with an FEI Quanta 200 scanning electron microscope at an accelerating voltage of 15.0 kV under high vacuum. The NP samples were imaged with aluminum specimen mounts with a 1/2″ slotted head and 1/8″ pin (Ted-Pella).

Cell culture. All cells were cultured and maintained at 37 °C in a humidified incubator containing 5% CO_2.

OVCAR8-GFP cells were cultured in Dulbecco's modified Eagle's medium (DMEM) (Invitrogen) supplemented with 10% FBS (Gemini Bio), 1% L-glutamine (Invitrogen), and 1% penicillin–streptomycin (Invitrogen). The cells were stably transduced with eGFP.

SKOV-3 cell line was obtained from American Type Culture Collection (ATCC) and was cultured, according to the ATCC protocol, in ATCC-formulated McCoy's 5a Medium Modified (ATCC) supplemented with 10% FBS. The cells were stably transduced with eGFP to become GFP-expressing cells (SKOV-3-GFP). When the cells reached 80% confluency, they were passaged using a 0.25% trypsin/EDTA solution (Invitrogen); media was changed every 2 to 3 d.

Imaging. Spectral Ami-X in vivo fluorescent whole-body imaging system was used to image the mice and the organs removed from the i.p. cavity (Spectral Instruments Imaging). The tumors were imaged at excitation (Ex) of 465 nm, emission (Em) of 510 nm, and red fluorescently labeled NPs were imaged at Ex of 570 nm and Em of 610 nm.

Confocal microscopic images were taken on a Zeiss LSM700 confocal microscope at 40×, 20×, and 10×.

Leica Z16 dissection Macroscope was used to image the tissues that removed from the i.p. cavity with GFP-green filter cube (BP 527/30) and TX-red filter cube (645/75).

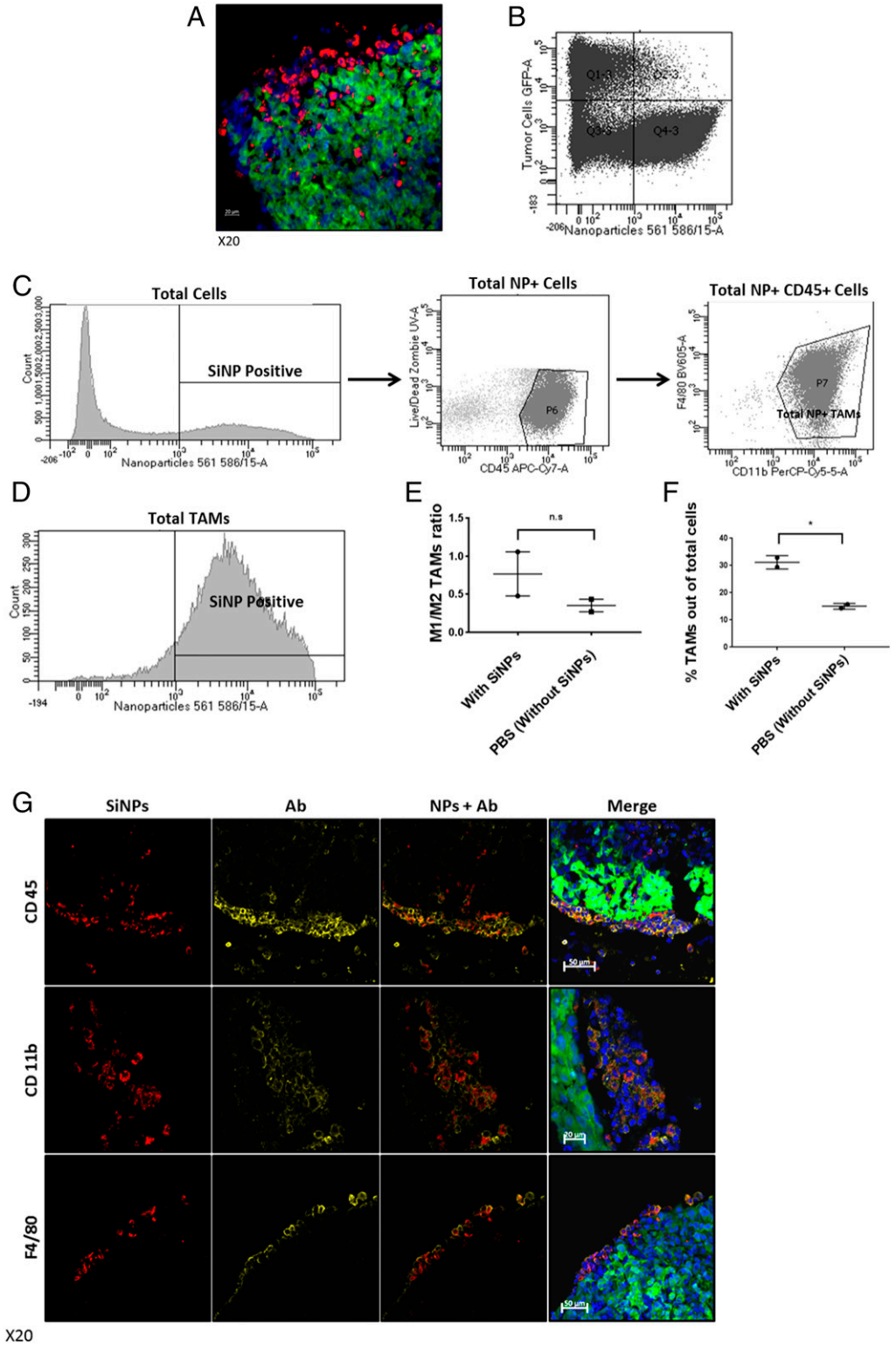

Fig. 4. Uptake of red fluorescent SiNPs by TAMs. EGFP-expressing human ovarian cancer cells (OVCAR8) were injected i.p. After 21 d, the red fluorescent-labeled SiNPs were injected i.p., and then 4 d later the animals were euthanized and tumors were removed and were prepared for either confocal imaging or flow cytometry (stained using anti-CD45, anti-CD11b, and anti-F4/80 antibodies). (*A*) Confocal image of representative sectioned tumor 4 d after i.p. injection of red fluorescent SiNPs. (Scale bar: 20 μm.) (*B*) Flow cytometry scatterplot of cancer cells (EGFP-expressing cancer cells) and cells that uptake the NPs showing that the cells that uptake the NPs are not cancer cells (2.1% of tumor cells contained SiNPs). (*C*) The percentage of cells in the tumor microenvironment containing SiNPs that are TAMs (72% of NP^+ cells were positive for CD45, CD11b, and F4/80). (*D*) The percentage of TAMs (positive for CD45, CD11b, and F4/80) out of total TAMs population in the tumor microenvironment that uptake SiNPs (87% on average). (*E*) M1/M2 ratio of TAMs in the tumor microenvironment in mice treated with SiNPs or PBS (ctrl). (M1 was characterized by an anti-iNOS antibody; M2 was characterized by an anti-CD206 antibody, n.s.) (*F*) Total number of TAMs in the tumor microenvironment in mice treated with SiNPs or PBS (ctrl); $P = 0.01$. (*G*) Confocal image of representative sectioned tumors (SiNPs, red; tumors, green; DAPI-stained nuclei, blue; anti-CD45, anti-CD11b, and anti-F4/80 antibody staining yellow to identify TAMs). Note merged images in far-right panels showing colocalization of SiNPs and macrophages at tumor surface. (Scale bar: 50 μm.)

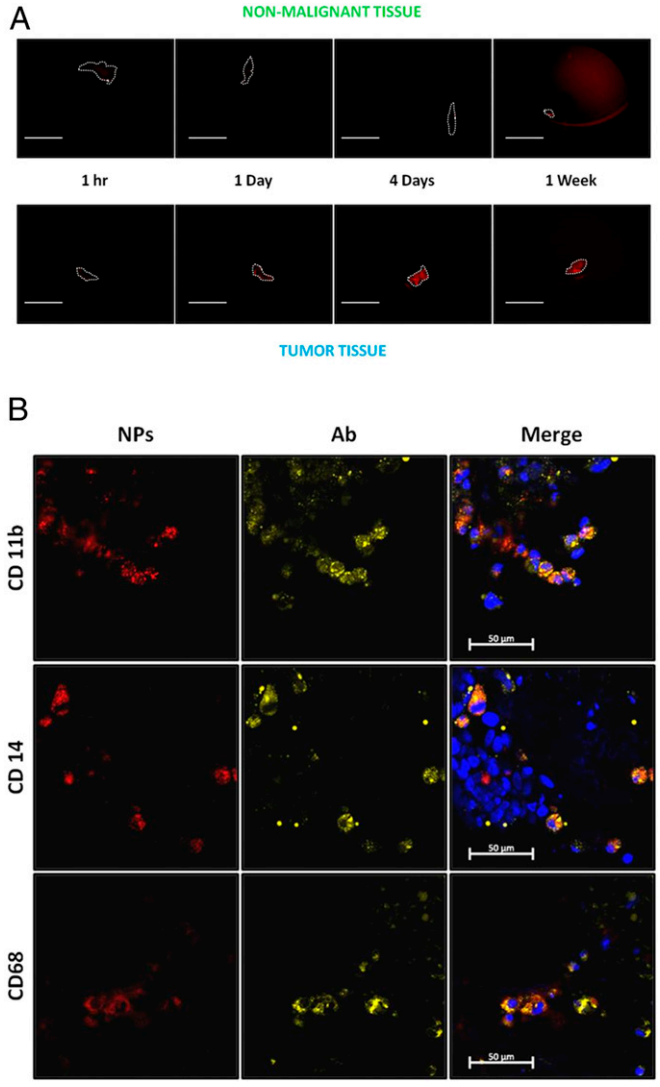

Fig. 5. Red fluorescent SiNPs can selectively detect human tumors by TAM uptake mechanism. (*A*) Fresh tumors and nonmalignant tissues were obtained from patients and incubated ex vivo with red fluorescent SiNPs and imaged with Leica Z16 dissection macroscope after 1 h, and 1, 4, and 7 d. (Scale bar: 1.0 cm.) (*B*) Confocal images of representative sectioned tumors after 4 d of incubation with SiNPs (red), DAPI tumor nuclei (blue), anti-CD11b (myeloid cells marker), anti-CD14 (monocytes and macrophages marker), and anti-CD68 (myeloid cells marker) antibodies to identify TAMs (yellow). (Scale bar: 50 μm.)

CryoVis (BioInVision) technology was used according to the company's protocols. This cryo-imaging system enables to acquire three-dimensional high-resolution color and fluorescence episcopic images by alternating between sectioning and imaging. CryoVis allows a whole-mouse imaging and can map fluorescent imaging agents at very high resolution and sensitivity.

NP Synthesis.

Au@SiNP preparation. Au@SiNPs were synthesized using a standard Stober protocol for SiNPs synthesis. Two milliliters of isopropanol were added to 9×10^{10} 50-nm gold NPs in 400 μL of water, and then 50 μL of ammonium hydroxide and 3.9 μL of tetraethyl-orthosilicate (TEOS) were added while stirring. After stirring for 1 h at room temperature (RT), the NPs were centrifuged and washed three times with MilliQ water.

Amine-SiNP nanoparticles. A 25-mL round-bottom flask with a magnetic stirring bar was flushed with nitrogen for 10 min. A dispersion of red SiNPs (500 nm, 3.8×10^{11} NPs) in 4 mL of ethanol was added to the flask under nitrogen followed by the addition of 0.67 mL of aqueous ammonia. The final NP concentration was 10 g/L in the solution mixture with a final ammonia concentration of 4 vol%. (3-Aminopropyl)triethoxysilane (APTES) (1 μL) in 0.33 mL of EtOH was then added to the reaction mixture and it was stirred at RT overnight. The amount of APTES was calculated under the assumption that each APTES molecule takes up 0.6 nm^2 on the NP surface. To ensure the complete conversion of the hydroxyl groups to amine groups on the NP surface, a sevenfold excess of APTES was used in the reaction. The following day, the reaction was refluxed at 85 °C while stirring for 2 h. The resulting NPs in the dispersion were collected and washed by repeated centrifugation at 21,000 × *g*, 1 min (three washes in EtOH, followed by three washes in MilliQ water). SiNP-NH_2 was redispersed in MilliQ water and stored at 4 °C.

PEG-SiNP nanoparticles. A water dispersion of SiNP-NH_2 containing 1.9×10^{11} NPs was exchanged to PBS solution by three repeated centrifugation cycles at 21,000 × *g*, 1 min in PBS. A 25-fold molar excess of sulfo-SMCC solution in PBS was added to the SiNP-NH_2, and the mixture was shaken at 37 °C for 1 h. To remove the salts and excess sulfo-SMCC, SiNPs were pelleted and washed three times with MilliQ water by centrifugation (21,000 × *g*, 1 min). The resulting SiNP-Mal particles were redispersed in MilliQ water and washed three times with PBS to convert their solvent to PBS followed by the addition of a PEG-SH solution in PBS. The mixture was placed in a shaker and incubated at 37 °C overnight. It was assumed that each maleimide group on the NP surface takes up 0.6 nm^2 and each maleimide functional group reacts with one thiol group on the PEG-SH molecules. To maximize PEG coverage on the NP surface, 10-fold molar excess of PEG-SH to the number of maleimide groups on the SiNP surface was used in the reaction. Upon reaction completion, PEGylated SiNPs were collected and washed by repeated centrifugation at 21,000 × *g* for 1 min (three times with MilliQ water). PEGylated SiNPs were resuspended in MilliQ water and stored at 4 °C.

PLGA NPs. PLGA particles were prepared using a protocol described (17). Briefly, 200 mg of PLGA (50:50; molecular weight, 30,000 to 60,000) and 2 mg of Nile Red were dissolved in 5 mL DCM. This mixture was then added to 20 mL of 5% PVA in water and homogenized for 30 s on high speed using a tabletop homogenizer in order to form an oil-in-water emulsion. This emulsion was then added to 100 mL of distilled water and allowed to stir covered at low speed for 1 h at RT. After 1 h, the solution is allowed to stir for another 2 h at RT uncovered to evaporate off the solvents. The NPs were collected by centrifugation (1,500 × *g* for 5 min) and washed three times with distilled water at the same settings. PLGA particles were resuspended in MilliQ water and stored at 4 °C.

Animal Experiments. All animals were maintained under specific pathogen-free conditions at the City of Hope Animal Resource Center, an AAALAC International accredited facility, and all procedures were reviewed and approved by the City of Hope Animal Care and Use Committee. AAALAC uses the *Guide for the Care and Use of Laboratory Animals* (18) for its accreditation standard.

Different surface counting and charge. Female, athymic nude mice (Charles River) that were 7 wk old were inoculated with 2 million OVCAR8-GFP cells via i.p. injection. After 21 d, mice ($n = 5$ per group) were i.p. injected with: 1.37×10^{10} 500-nm red fluorescently labeled hydroxyl-SiNP (Micromod Partikeltechnologie GmbH) in 1 mL of PBS, 1.37×10^{10} amine-red-fluorescently labeled SiNP in 1 mL of PBS, or 1.37×10^{10} PEG-red-fluorescently labeled SiNP in 1 mL of PBS. Control mice received 1 mL of PBS injection. After 4 d, the mice were euthanized, the organs in the i.p. cavity were removed, and a fluorescent whole-body imaging system was used (Spectral Ami-X; Spectral Instruments Imaging). The tumors and adjacent healthy tissues were then removed and prepared for confocal imaging.

Kinetics of attachment. Female, athymic nude mice (Charles River) that were 7 wk old were inoculated with 2 million OVCAR8-GFP cells via i.p. injection. After 21 d, mice ($n = 4$ per group) were i.p. injected with 1.37×10^{10} 500-nm red-fluorescently labeled SiNP (Micromod Partikeltechnologie GmbH) in 1 mL of PBS. Control mice received 1-mL PBS injection. After 1 h, 5 h, 24 h, and 4 d, the mice were euthanized, the organs in the i.p. cavity were removed, and a fluorescent whole-body imaging system was used (Spectral Ami-X; Spectral Instruments Imaging). The tumors and adjacent healthy tissues were then removed and prepared for confocal imaging.

Different size assessment. Female, athymic nude mice (Charles River) that were 7 wk old were inoculated with 2 million OVCAR8-GFP cells via i.p. injection. After 21 d, mice ($n = 5$ per group) were i.p. injected with 10-, 50-, 200-, 500-, and 1,000-nm red-fluorescently labeled SiNP (Micromod Partikeltechnologie GmbH) in 1 mL of PBS (HD size measured by DLS: 24.6, 54.7, 194.8, 443.9, and 982.9 nm, and ζ-potential measured: −24.22, −23.19, −37.12, −54.59, and −73.71 mV). Control mice received 1-mL PBS injection. All of the NP samples were compared and normalized based on their fluorescence intensity as measured by a fluorimeter, and not by NP number (as was done in other experiments) or mass. Since both the Spectral Ami-X and the Leica Z16

dissection macroscope measure the fluorescence intensity, normalizing the injected dose by NPs number will be favored for the large NPs, and normalizing the groups by mass will be favored for the small NPs. After 4 d, the mice were euthanized, the organs in the i.p. cavity were removed, and a fluorescent whole-body imaging system was used (Spectral Ami-X; Spectral Instruments Imaging). The organs from the i.p. cavity were also imaged by Leica Z16 dissection macroscope. The tumors and adjacent healthy tissues were then removed and prepared for confocal imaging.

Administration route assessment. Female, athymic nude mice (Charles River) that were 7 wk old were inoculated with 2 million OVCAR8-GFP cells via i.p. injection. After 21 d, mice ($n = 5$ per group) were i.p. injected with 1.37×10^{10} red-fluorescently labeled SiNP (Micromod Partikeltechnologie GmbH) in 1 mL of PBS. Control mice received 1-mL PBS injection. The i.v. administration group was i.v. injected to the tail vein with 1.52×10^{9} (1 mg/mL) 500-nm red-fluorescently labeled SiNP in 0.2 mL of PBS. Control mice of that group received 0.2-mL PBS injection. The i.v. administration group received a lower amount of NPs since it is not recommended to inject i.v. more than 0.2 mL and higher concentrations than 1 mg/mL. After 4 d, the mice were euthanized, the organs in the i.p. cavity were removed, and a fluorescent whole-body imaging system was used (Spectral Ami-X; Spectral Instruments Imaging). The organs from the i.p. cavity were also imaged by Leica Z16 dissection macroscope. The tumors and adjacent healthy tissues were then removed and prepared for confocal imaging.

Different ovarian cancer cell lines. Female, athymic nude mice (Charles River) that were 7 wk old were inoculated with 2 million OVCAR8-GFP or Skov-3-GFP cells via i.p. injection. After 21 d, mice ($n = 5$ per group) were i.p. injected with 1.37×10^{10} 500-nm red-fluorescently labeled SiNP (Micromod Partikeltechnologie GmbH) in 1 mL of PBS. Control mice received 1-mL PBS injection. After 4 d, the mice were euthanized, the organs in the i.p. cavity were removed, and a fluorescent whole-body imaging system was used (Spectral Ami-X; Spectral Instruments Imaging). The organs from the i.p. cavity were also imaged by Leica Z16 dissection macroscope. The tumors and adjacent healthy tissues were then removed and prepared for confocal imaging.

In vivo biodistribution study. Female, athymic nude mice (Charles River) that were 7 wk old were inoculated with 2 million OVCAR8-GFP cells via i.p. injection. After 21 d, mice ($n = 4$ per group) were i.p. injected with 1.37×10^{10} Au@SiNPs in 1 mL of PBS. Control group received 1-mL PBS injection. After 4 d, the mice were euthanized and the liver, spleen, kidneys, stomach, lungs, intestines, and tumors were collected from the peritoneal cavity of each animal from each treatment group and placed into 50- or 15-mL metal-free plastic tubes. The samples were stored in a −20 °C freezer until preparation for ICP-MS analysis. For ICP-MS analysis, the samples were digested directly in the tubes by adding a mixture of concentrated acids (68% HNO_3, 1% HCl, 0.2% HF) and incubating overnight in an oil bath at 80 °C (*SI Appendix*, Table S1). As a control for the total amount of Au@SiNPs injected per mouse (100% injected dose), the same volume and concentration of Au@SiNPs injected was similarly digested. The samples were serially diluted 1,000-fold with a 2% HNO_3 1% HCl solution to minimize the final concentration of HF, and then analyzed on an Agilent 8800 ISIS in no gas mode to determine gold concentration. The total amount of gold was calculated by multiplying the measured concentration (in parts per billion) with the total volume of sample after dilutions, then normalized to the 100% injected dose of Au@SiNPs.

Polystyrene in vivo study. Female, athymic nude mice (Charles River) that were 7 wk old were inoculated with 2 million OVCAR8-GFP cells via i.p. injection. After 21 d, mice ($n = 5$ per group) were i.p. injected with polystyrene NPs loaded with Nile Red (SPHERO Fluorescent Particles FP-3056-2; Sphereotech). These particles had an effective particle diameter of 798 nm (0.0137 polydispersity index value) and surface charge of (-21.32 ± 3.20 mV) as assessed by DLS and ζ-potential measurements ($n = 5$). Control mice received 1-mL PBS injection. After 4 d, the tumors and adjacent healthy tissues were removed and prepared for confocal imaging.

Immunofluorescent staining. Organs collected from the i.p. cavity were placed in 4% PFA solution for 3 d at 4 °C in the dark, washed with PBS three times, and stored in 30% sucrose solution at 4 °C for 3 d. The tissues were embedded in optimal cutting temperature medium just prior to sectioning using a cryostat. The sections thickness was 10 μm, and they were mounted on Superfrost Plus slides (Thermo Fisher Scientific) and stored at −20 °C. All sections were blocked for 30 min at RT with blocking solution (PBS containing 1% BSA, 10% FBS, 0.2% Saponin). Sections were then incubated overnight at 4 °C with the primary antibodies diluted in blocking buffer: rat anti-mouse CD11b (Biolegend), rat anti-mouse F4/80 (Biolegend), rat anti-mouse GR1 (BD Biosciences), rat anti-mouse CD45 (Biolegend), rat anti-human CD11b (Biolegend), mouse anti-human CD68 (Biolegend), and mouse anti-human CD14 (Biolegend).

Sections were washed five times with PBST for 5 min each and incubated with the secondary antibody for 1 h at RT: Alexa Fluor 647 goat anti-rat (Invitrogen) or Alexa Fluor 647 goat anti-mouse (Biolegend).

Sections were then washed three times with PBST for 5 min each and stained with DAPI solution for 5 min at RT. Sections were then washed three times with PBST for 5 min each.

Fluorescence mounting medium (Dako) was applied before slides were coverslipped and stored at 4 °C until imaging.

In vivo biodistribution study–CryoVis. Female, athymic nude mice (Charles River) that were 7 wk old were inoculated with 2 million OVCAR8-GFP cells via i.p. injection. After 21 d, mice were i.p. injected with 1.37×10^{10} red-fluorescently labeled SiNP (Micromod Partikeltechnologie GmbH) in 1 mL of PBS. Control group (untreated tumor-bearing mouse) received 1-mL PBS injection. Healthy mice group (without tumors) were i.p. injected, at day 21, with 1.37×10^{10} red-fluorescently labeled SiNP (Micromod Partikeltechnologie GmbH) in 1 mL of PBS. After 4 d, the mice were euthanized and cryofrozen according to the company's protocols, and shipped to BioInVision for imaging and analysis.

Human Tissue Procurement and Processing. Fresh tumors and nonmalignant tissues were obtained from patients who gave informed consent before tissue collection at the City of Hope Medical Center. This study was approved by the City of Hope institutional review board (IRB) (City of Hope [COH] IRB 15280). The fresh tumors and nonmalignant tissues were incubated in 1.5 mg/mL solution of 500-nm red fluorescently labeled SiNP (Micromod Partikeltechnologie GmbH) in 4 mL of DMEM media. One hour and 1, 4, and 7 d later, the tissues were washed in PBS three times and were placed in a new plate and imaged with the Leica Z16 dissection macroscope. The preparation of human tumors for confocal imaging was done the same way as the preparation of mice organs for confocal imaging.

Statistical Analysis. Results are presented as mean ± SD, unless otherwise stated. Statistical significance between different groups was determined by ANOVA followed by Bonferroni-corrected post hoc *t* tests.

Data Sharing. Additional data such as additional images or underlying measurement data files are available upon request.

ACKNOWLEDGMENTS. We gratefully acknowledge the following: TEM imaging was conducted at the Electron Microscopy Core with Marcia Millier, Zhuo Li, and Ricardo Zerda; fluorescent imaging was conducted at the Digital and Light Microscopy Core with Brian Armstrong and Loren Quintanar; Nanosight measurements were conducted at the Analytical Cytometry Core with Lucy Brown; and wide-field imaging was conducted at the Small Animal Imaging Core with Dr. David Colcher and Desiree Lasiewski. Studies were supported by generous funding from STOP Cancer, The Rosalinde and Arthur Gilbert Foundation, the Alvarez Family Foundation, The Anthony F. and Susan M. Markel Foundation, Jeanne and Bruce Nordstrom, and the NIH (Grant R01 CA197359). T.H. was supported by a fellowship from the Israel–City of Hope fellowship program in biomedical research; R.M. was supported by a fellowship from the California Institute for Regenerative Medicine (CIRM) (Grant TG2-01150) and the Ladies Auxiliary of the Veterans of Foreign Wars; M.G. was supported by the CIRM Bridges Training Program (Grant TB1-01177). The contents of this publication are solely the responsibility of the authors and do not necessarily represent the official views of CIRM or any other agency of the State of California. Materials transfer information is available from the City of Hope Office of Technology Licensing (www.cityofhope.org/research/support/center-for-applied-technology-development/office-of-technology-licensing/Pages/default.aspx). Research reported in this publication included work performed in cores supported by the National Cancer Institute of the NIH under Award P30 CA033572. The content is solely the responsibility of the authors and does not necessarily represent the official views of the NIH.

1. M. Zhang *et al.*, A high M1/M2 ratio of tumor-associated macrophages is associated with extended survival in ovarian cancer patients. *J. Ovarian Res.* **7**, 19 (2014).
2. ACS, Survival rates for ovarian cancer. https://www.cancer.org/cancer/ovarian-cancer/about/key-statistics.html. Accessed 22 July 2020.
3. N. Auslander *et al.*, Robust prediction of response to immune checkpoint blockade therapy in metastatic melanoma. *Nat. Med.* **24**, 1545–1549 (2018).
4. S. L. Gaillard, A. A. Secord, B. Monk, The role of immune checkpoint inhibition in the treatment of ovarian cancer. *Gynecol. Oncol. Res. Pract.* **3**, 11 (2016).

5. C. B. Rodell *et al*., TLR7/8-agonist-loaded nanoparticles promote the polarization of tumour-associated macrophages to enhance cancer immunotherapy. *Nat. Biomed. Eng.* **2**, 578–588 (2018).
6. A. Mantovani, F. Marchesi, A. Malesci, L. Laghi, P. Allavena, Tumour-associated macrophages as treatment targets in oncology. *Nat. Rev. Clin. Oncol.* **14**, 399–416 (2017).
7. J. W. Pollard, Trophic macrophages in development and disease. *Nat. Rev. Immunol.* **9**, 259–270 (2009).
8. M. Yin *et al*., Tumor-associated macrophages drive spheroid formation during early transcoelomic metastasis of ovarian cancer. *J. Clin. Invest.* **126**, 4157–4173 (2016).
9. S. Wilhelm *et al*., Analysis of nanoparticle delivery to tumours. *Nat. Rev. Mater.* **1**, 16014 (2016).
10. P. Cao *et al*., Intraperitoneal administration of neural stem cell-nanoparticle conjugates targets chemotherapy to ovarian tumors. *Bioconjug. Chem.* **28**, 1767–1776 (2017).
11. Z. Lu *et al*., Tumor-penetrating microparticles for intraperitoneal therapy of ovarian cancer. *J. Pharmacol. Exp. Ther.* **327**, 673–682 (2008).
12. T. Kamei *et al*., Spatial distribution of intraperitoneally administrated paclitaxel nanoparticles solubilized with poly(2-methacryloxyethyl phosphorylcholine-co *n*-butyl methacrylate) in peritoneal metastatic nodules. *Cancer Sci.* **102**, 200–205 (2011).
13. D. Soma *et al*., Intraperitoneal administration of paclitaxel solubilized with poly(2-methacryloxyethyl phosphorylcholine-co *n*-butyl methacrylate) for peritoneal dissemination of gastric cancer. *Cancer Sci.* **100**, 1979–1985 (2009).
14. A. J. Di Pasqua *et al*., Neutron-activatable holmium-containing mesoporous silica nanoparticles as a potential radionuclide therapeutic agent for ovarian cancer. *J. Nucl. Med.* **54**, 111–116 (2013).
15. A. H. Colby *et al*., Highly specific and sensitive fluorescent nanoprobes for image-guided resection of sub-millimeter peritoneal tumors. *ACS Nano* **11**, 1466–1477 (2017).
16. J Feng *et al*., Effects of size and targeting ligand on biodistribution of liposome nanoparticles in tumor mice. *J. Nucl. Med. Meeting Abstracts* **54**, 1339 (2013).
17. P. Xu *et al*., Intracellular drug delivery by poly(lactic-*co*-glycolic acid) nanoparticles, revisited. *Mol. Pharm.* **6**, 190–201 (2009).
18. National Research Council, *Guide for the Care and Use of Laboratory Animals*, (National Academies Press, Washington, DC, 8th Ed., 2011).